Compressive response of $Ni_{45.3}Ti_{34.7}Hf_{15}Pd_5$ and $Ni_{45.3}Ti_{29.7}Hf_{20}Pd_5$ shape-memory alloys

E. Acar · H. Tobe · I. Kaya · H. E. Karaca ·
Y. I. Chumlyakov

Abstract The shape-memory properties of $Ni_{45.3}Ti_{34.7}$ $Hf_{15}Pd_5$ and $Ni_{45.3}Ti_{29.7}Hf_{20}Pd_5$ polycrystalline alloys were determined through superelasticity and shape-memory tests in compression. It has been revealed that the $Ni_{45.3}Ti_{34.7}Hf_{15}Pd_5$ has a maximum transformation strain of 3.8 % and work output of up to 30 J cm^{-3}, while the $Ni_{45.3}Ti_{29.7}Hf_{20}Pd_5$ has a maximum transformation strain of 2.6 % and work output of up to 20 J cm^{-3} at 700 MPa. Two-way shape-memory strains of 0.6 and 0.85 % were obtained in $Ni_{45.3}Ti_{34.7}Hf_{15}Pd_5$ and $Ni_{45.3}Ti_{29.7}Hf_{20}Pd_5$ alloys, respectively. The $Ni_{45.3}Ti_{34.7}Hf_{15}Pd_5$ showed superelasticity at 90 °C with recoverable strain of 3.1 %, while high hardening of $Ni_{45.3}Ti_{29.7}Hf_{20}Pd_5$ limited its superelastic behavior. Microstructure of the $Ni_{45.3}Ti_{34.7}$ $Hf_{15}Pd_5$ alloy was revealed by transmission electron microscopy, and effects of composition on the lattice parameters of the transforming phases and martensite morphology were discussed.

E. Acar · H. Tobe · I. Kaya · H. E. Karaca (✉)
Department of Mechanical Engineering, University of Kentucky,
Lexington, KY 40506, USA
e-mail: karacahaluk@uky.edu

E. Acar
Aircraft Engineering, Erciyes University, Melikgazi,
38039 Kayseri, Turkey

I. Kaya
Department of Mechanical Engineering, Faculty of Engineering,
Anadolu University, 26555 Eskisehir, Turkey

Y. I. Chumlyakov
Siberian Physical-Technical Institute at Tomsk State University,
Tomsk 634050, Russia

Introduction

Shape-memory alloys (SMAs) are attractive class of functional materials with unique properties (e.g., shape-memory effect and superelasticity, SE) owing to their ability to undergo a thermoelastic martensitic transformation [1]. Very high strains, work outputs, and low hysteresis in actuation in addition to noise reduction and vibration damping are some outcomes of the SMAs [2–4]. They are also lightweight, frictionless, and easy to inspect [5–7]. Among the SMAs, NiTi alloys are the center of attention due to their good functional and mechanical properties [8, 9]. Thus, NiTi alloys have been used in numerous applications in many industries including automotive, aerospace, oil–gas [10], medical [11–13], construction, and seismic protection [11, 14].

However, the most studied NiTi system, near-equiatomic NiTi alloys, have certain disadvantages such as low transformation temperatures (TTs) (<100 °C) and strength (<700 MPa) [5, 15], which preclude their use in applications requiring high temperature and high strength. Hence, ternary alloying is employed to improve its shape-memory properties, where several NiTi–X (X = Pd, Hf, Pt, Zr) alloy systems have been investigated to date [16]. NiTiHf alloys are of high interest due to increased TTs and the lower cost of Hf compared to other precious metals [17] of Pd and Pt. However, there are also several disadvantages of Ni-lean NiTiHf alloys such as large thermal hysteresis (results in additional energy requirements and cycle time in actuator applications), poor thermal stability, brittleness, and low strength impeding their superelastic behavior [18]. All together, these shortcomings seriously limit the potential of Ni-lean NiTiHf alloys for practical applications. However, it has been recently demonstrated that precipitation-hardened Ni-rich NiTiHf alloys are promising alloys for high-

temperature applications since they have high TTs, high strength, and low thermal hysteresis [19, 20].

Quaternary alloying can also be employed to alleviate the aforementioned limitations in the ternary alloys. Previously, shape-memory properties of $Ni_{45.3}Ti_{29.7}Hf_{20}Pd_5$ (at.%) were investigated as functions of aging temperature and time in polycrystalline [21] and single crystal [22–24] forms. It was shown that the [111]-oriented solutionized single crystals show superelastic behavior under extremely high stress levels (2.5 GPa) with low plastic deformation in addition to a very large damping capacity (44 J cm^{-3}) due to a very wide mechanical hysteresis (>1200 MPa) [22]. The aged $Ni_{45.3}Ti_{29.7}Hf_{20}Pd_5$ polycrystalline has recoverable shape-memory strain of up to ∼4 % under 1000 MPa, while [111]-oriented $Ni_{45.3}Ti_{29.7}Hf_{20}Pd_5$ single crystals exhibited ∼2 % strain at stress levels as high as 1500 MPa [24].

Previously, shape-memory properties of a homogenized $Ni_{45.3}Ti_{39.7}Hf_{10}Pd_5$ (at.%) alloy system were reported [25], where transformation strain of up to 4.6 % and work output of up to 29 J cm^{-3} were obtained from strain–temperature responses. $Ni_{45.3}Ti_{39.7}Hf_{10}Pd_5$ showed a perfect superelastic behavior at 90 °C with recoverable strain of 4.3 %. It was also determined that the $Ni_{45.3}Ti_{39.7}Hf_{10}Pd_5$ alloy could develop two-way shape-memory strain of 1.6 % after thermal cycling under stress experiments [25]. In this study, in order to reveal the effects of Hf content on the shape-memory properties of NiTiHfPd alloys, the shape-memory behavior (including two-way shape-memory effect, TWSME) and superelastic responses of homogenized $Ni_{45.3}Ti_{34.7}Hf_{15}Pd_5$ and $Ni_{45.3}Ti_{29.7}Hf_{20}Pd_5$ (at.%) polycrystalline SMAs were investigated in compression, and they were compared to the homogenized $Ni_{45.3}Ti_{39.7}Hf_{10}Pd_5$ alloys.

Materials and methods

The arc melting method was used to fabricate the $Ni_{45.3}Ti_{34.7}Hf_{15}Pd_5$ and $Ni_{45.3}Ti_{29.7}Hf_{20}Pd_5$ (at.%) alloy ingots, starting with high-purity elemental constituents; [99.98 wt% Ni; 99.995 wt% Pd, 99.95 wt% Ti and 99.7 wt% Hf (excluding Zr, which is nominally 3 %)], $Ni_{45.3}Ti_{39.7}Hf_{10}Pd_5$, $Ni_{45.3}Ti_{34.7}Hf_{15}Pd_5$, and $Ni_{45.3}Ti_{29.7}Hf_{20}Pd_5$ alloys will be referred as NiTiPd–10Hf, NiTiPd–15Hf, and NiTiPd–20Hf, respectively, throughout the text for brevity. The ingots were homogenized at 900 °C for 72 h in vacuum followed by a furnace cooling process. Compression samples ($4 \times 4 \times 8$ mm^3) were electro-discharge machined from the homogenized ingots. Differential Scanning Calorimetry (DSC) technique was used to measure the TTs using a Perkin-Elmer Pyris 1 DSC with heating and cooling rates of 10 °C min^{-1} at stress-free condition. The TTs calculated by the intersection method of the three alloys under stress-free conditions are shown in Table 1.

Table 1 Transformation Temperatures of the NiTiPd–10Hf, NiTiPd–15Hf, and NiTiPd–20Hf alloys obtained through DSC measurements

Material	Martensite finish, M_f (°C)	Martensite start, M_s (°C)	Austenite start, A_s (°C)	Austenite finish, A_f (°C)
NiTiPd–10Hf	−40	−4	1	45
NiTiPd–15Hf	35	50	63	106
NiTiPd–20Hf	75	110	102	150

Mechanical testing was conducted in an MTS Landmark servo hydraulic test platform with 100 kN load cell. The thermal cycling experiments were performed with 10 °C min^{-1} heating and cooling rates at constant stress, while SE experiments were performed with 8×10^{-4} mm s^{-1} loading and 100 N s^{-1} unloading rates at constant temperature.

In the thermal cycling experiments, stresses ranging from 25 to 1000 MPa were applied in compression above the A_f, and then the samples were cooled down below the M_f and heated back above A_f under the constant stress. On the other hand, in SE experiments, the specimens were loaded to a selected compressive strain and then unloaded at constant temperatures above A_f. Transmission electron microscope (TEM) observations were conducted at room temperature (RT) in a JEOL 2010F instrument operated at 200 kV. The specimens for TEM observation were prepared by a twin-jet polishing technique using a solution of 20 % sulfuric acid and 80 % methanol at around −15 °C (258 K).

Results and discussion

Micro- and crystal structure of NiTiPd–15Hf and NiTiPd–20Hf alloys

Figure 1a shows the X-ray diffraction patterns of NiTiPd–10Hf, NiTiPd–15Hf, and NiTiPd–20Hf alloys at RT. All the alloys consist of two phases, B2 austenite and B19′ martensite at room temperature. The crystal structure of NiTiPd–10Hf austenite was B2 cubic with $a = 0.3063$ nm, and the crystal structure of martensite is B19′ monoclinic with lattice parameters of $a = 0.2985$ nm, $b = 0.4127$ nm, $c = 0.4732$ nm, and $\beta = 99.3°$. For NiTiPd–15Hf, the crystal structure of the martensite was B19′ with lattice parameters of $a = 0.3034$ nm, $b = 0.4109$ nm, $c = 0.4805$ nm, and $\beta = 100.9°$, while the lattice parameter of B2 austenite phase was $a = 0.3085$ nm. On the other hand, the NiTiPd–20Hf had a B19′ martensite with lattice parameters of $a = 0.3072$ nm, $b = 0.4128$ nm, $c = 0.4892$ nm, and $\beta = 102.6°$, while the B2 austenite had a lattice parameter of $a = 0.3121$ nm. Thus, it can be concluded that as the Hf content increased, lattice parameters of the
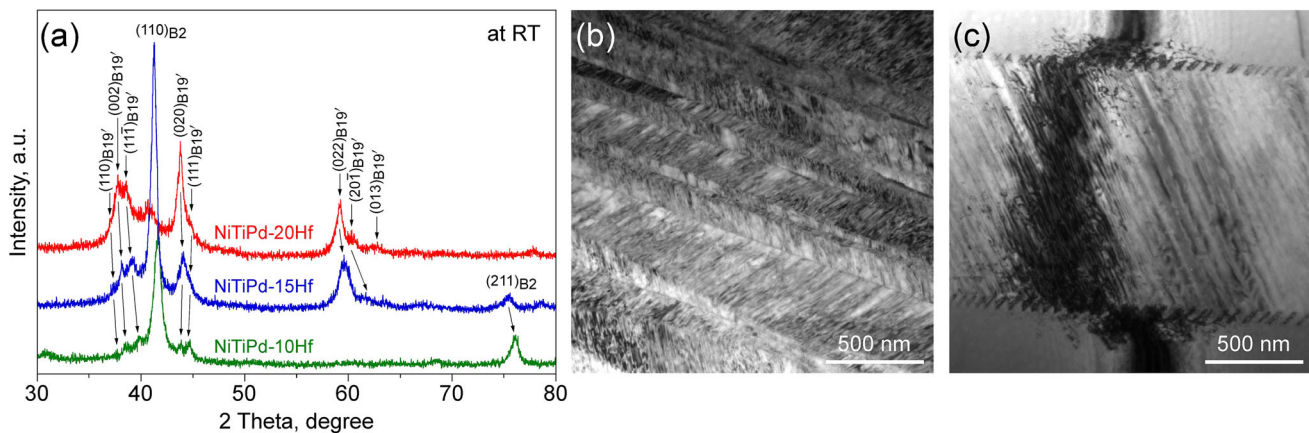
Fig. 1 **a** X-ray diffraction patterns for the NiTiPd–10Hf, NiTiPd–15Hf, and NiTiPd–20Hf alloys. Bright-field TEM images of the **b** NiTiPd–15Hf alloy and **c** NiTiPd–10Hf alloy

transforming phases are also increased in the current alloys. The volume of the B2 cubic structure of the austenite was expanded by 2.192 and 5.812 % as the Hf content was increased from 10 to 15 % and to 20 %, respectively.

Figure 1b and c shows the bright-field TEM micrographs of the NiTiPd–15Hf and NiTiPd–10Hf alloys, respectively. The thickness of the martensite plates of NiTiPd–15Hf is lower than that in NiTiPd–10Hf. The internal twin of the NiTiPd–15Hf was found to be $(001)_{B19'}$ compound twin which has also been observed in the NiTiPd–20Hf [21]. On the other hand, the internal twin of the NiTiPd–10Hf alloy was confirmed to be $\langle 011 \rangle_{B19'}$ type II twin [25]. It is noted that the thickness of the $(001)_{B19'}$ compound twin was thinner than that of the $\langle 011 \rangle_{B19'}$ type II twin and higher density of twins was observed in the NiTiPd–15Hf alloy.

The strain–temperature responses

The load biased shape-memory responses of the NiTiPd–15Hf alloy as a function of stress are shown in Fig. 2. Compressive stresses ranging from 25 to 1000 MPa were applied in austenite and kept constant during the thermal cycling. No irrecoverable strain was observed up to a stress level of 600 MPa.

Figure 3 shows that the shape-memory responses of the NiTiPd–20Hf alloy as a function of compressive stress ranging from 25 to 1000 MPa were applied. Irrecoverable strain was observed after 700 MPa.

Figure 4a shows the transformation strain values as functions of applied stress, extracted from the thermal cycling experiments shown in Figs. 2 and 3. Total strain was measured between the cooling and heating curves at M_s, as shown in Fig. 2b. As the applied stress is increased, the total strain is also increased and then saturated as the selection of preferred variants of martensite saturated at

intermediate stress levels. Beyond the plateau, with further increase in stress, transformation strain started to decrease due to plastic deformation.

Transformation strain was calculated by mathematically subtracting the irrecoverable strain from the total strain. Transformation strains were 0.3, 3.5, and 3 % under 25, 500, and 1000 MPa, respectively, for NiTiPd–15Hf, while transformation strains of 0, 2.2, and 2 % were observed in NiTiPd–20Hf under 25, 500, and 1000 MPa, respectively. For NiTiPd–10Hf, the transformation strains were 0.8, 4.6, and 5 % under 25, 500, and 1000 MPa, respectively [25]. It is clear that as the Hf content increased in the alloys, the transformation strains were decreased, which is in good agreement with the previously reported data for NiTiHf alloys [26].

The change of TTs (e.g., M_s and A_f) with applied stress in the strain–temperature responses (Figs. 2 and 3) are plotted in Fig. 4b, c, and d for the NiTiPd–10Hf, NiTiPd–15Hf, and NiTiPd–20Hf, respectively. It was found that Clausius–Clapeyron (C–C) slopes were 8.5, 11.8, and 15 MPa $^{\circ}C^{-1}$ for M_s in the NiTiPd–10Hf, NiTiPd–15Hf, and NiTiPd–20Hf alloys, respectively. The C–C relationship is formulated as [27]

$$\frac{\Delta\sigma}{\Delta T} = -\frac{\Delta H}{T_o\, \varepsilon_{tr}},$$

where $\Delta\sigma$ is the difference between critical stresses, ΔT is the temperature difference, ΔH is the transformation enthalpy, T_o is the equilibrium temperature, and ε_{tr} is the reversible strain. Assuming that the ΔH and T_o are comparable in these alloys, there is a good agreement between the C–C slopes and the transformation strains, ε_{tr} of the current alloys where the C–C slopes are inversely proportional to ε_{tr}.

Figure 5 shows the thermal hysteresis and irrecoverable strain values as a function of applied stress obtained from the strain–temperature responses. Figure 2b shows the

Fig. 2 The strain–temperature response of the NiTiPd–15Hf alloy as a function of stress from 25 to 1000 MPa
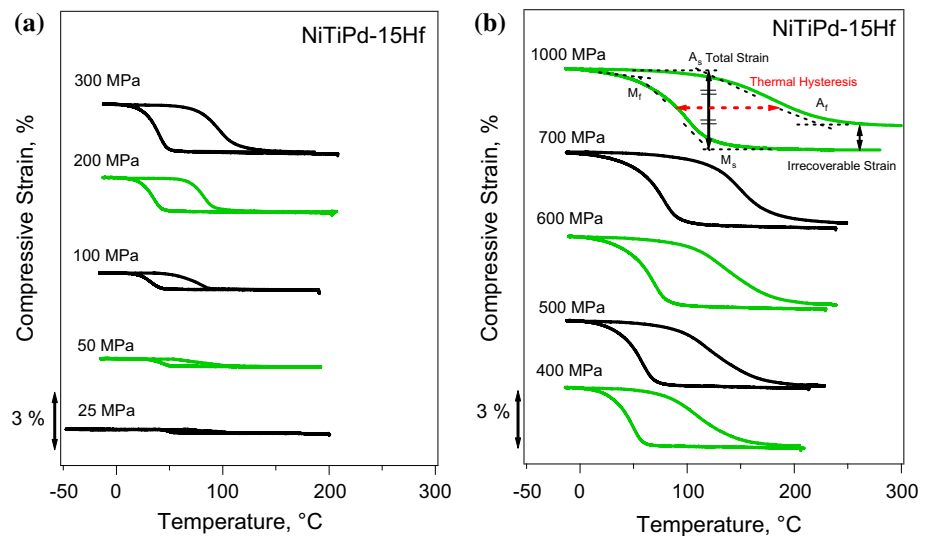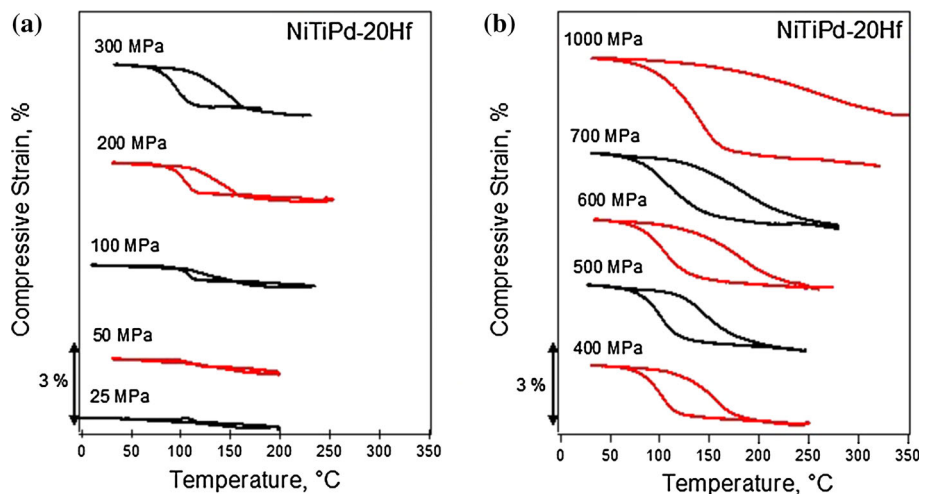

Fig. 3 The strain–temperature response of the NiTiPd–20Hf alloy as a function of stress from 25 to 1000 MPa

calculation methods of TTs, the thermal hysteresis, and the irrecoverable strain. The irrecoverable strain was not observed up to 500, 600, and 700 MPa in NiTiPd–10Hf, NiTiPd–15Hf, and NiTiPd–20Hf alloys, respectively. [25]. As the stress was increased to 1000 MPa, irrecoverable strains of 2.5, 1.3, and 1.8 % were measured for NiTiPd–10Hf alloy [25], NiTiPd–15Hf, and NiTiPd–20Hf alloys, respectively.

For NiTiPd–10Hf, the temperature hysteresis was almost constant (66 °C) up to 700 MPa. This was followed by a dramatic increase in hysteresis to 113 °C as the applied stress was increased to 1000 MPa [25]. The thermal hysteresis of the NiTiPd–15Hf was 39 and 66 °C under 25 and 500 MPa, respectively. Then, it increased to 105 °C under 1000 MPa. In the NiTiPd–20Hf, the hysteresis cannot be detected at 25 MPa, while it was increased from 48 °C to above 150 °C as the applied stress increased from

500 to 1000 MPa. Consequently, the increase of the Hf content resulted in lower initial temperature hysteresis, and the progress of the thermal hysteresis with stress was different.

The evolution of the thermal hysteresis in the current alloys can be analyzed in two regions as before (pre-saturation region) and after (post-saturation region) saturation stress. The saturation stress could be defined as the stress at which transformation strain stops increasing and starts either saturating or decreasing as shown in Fig. 4a. For instance, the saturation stress was 500 MPa for the NiTiPd–10Hf alloy, while it was 700 MPa for the NiTiPd–15Hf and NiTiPd–20Hf alloys. The thermal hysteresis in the NiTiPd–10Hf alloy was almost constant up to the saturation stress of 500 MPa where it increased progressively even before the saturation stress in the NiTiPd–15Hf and NiTiPd–20Hf alloys. After plastic deformation occurred
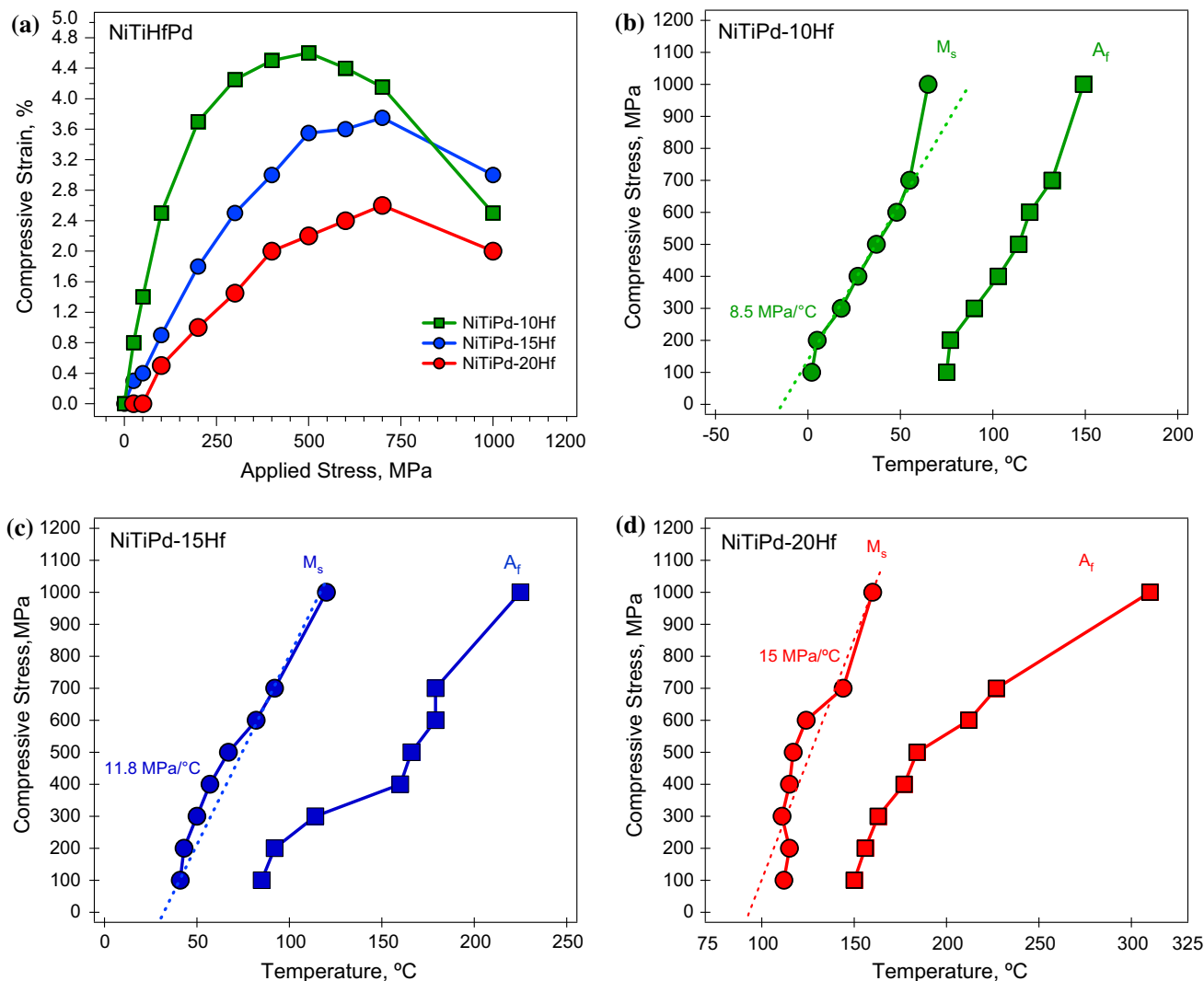
Fig. 4 a Transformation strain as a function of stress and b C–C relationship in NiTiPd–10Hf, c C–C relationship in NiTiPd–15Hf, and d C–C relationship in NiTiPd–20 alloys
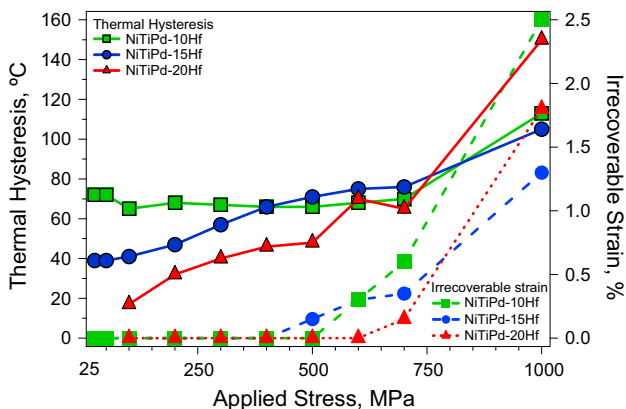

Fig. 5 Thermal hysteresis and irrecoverable strain as functions of applied stress extracted from the strain–temperature response of the NiTiPd-10Hf, NiTiPd-15Hf, and NiTiPd-20Hf alloys (data for NiTiPd–10Hf were taken from [25] for comparison)

(shown as increased irrecoverable strain in Fig. 5), hysteresis increased abruptly in all the alloys. It is known that the hysteresis is a result of dissipation mechanisms in SMAs [8, 28]. In SMAs, the three main energy dissipation mechanisms can be expressed as (i) friction between transforming phases or in-compatibility, (ii) friction between martensite variants and (iii) dislocation generation [29]. Friction during detwinning can also be added to the list.

When the stress is low initially, the difference between thermal hysteresis of the two alloys should be independent of possible effects associated with the applied stress. The thermal hysteresis was 72, 41, and 17 °C at 100 MPa for NiTiPd–10Hf, NiTiHf–15Hf, and NiTiPd–20Hf alloys, respectively.

This initial difference in the hysteresis could be related to the compatibility between the transforming phases of the

alloys. It has been reported that there is a close relationship between hysteresis and lattice compatibility that depends on the lattice parameters of the transforming phases in SMAs. When the interphase of the transforming phases is more compatible, a lower hysteresis is expected [30–32]. A sign of the compatibility between the transforming phases is the middle eigen value λ_2 of a selected matrix of the phase transformation between crystal structures based on the Non-Linear Geometric Theory of Martensite (NLGTM) [30]. According to the theory, the closer the middle Eigen value is to 1, the less hysteresis is expected in SMAs [31, 33–37]. Using the parameters for B2 to B19′ transformation [38], λ_2 values were calculated to be 0.9077, 0.8870, and 0.8747 for the NiTiHf–10Hf, NiTiPd–15Hf, and Ni-TiPd–20Hf, respectively. It is clear that there is an inverse relation between the middle Eigen values and the initial temperature hysteresis in the currently studied NiTiHfPd alloys. Moreover, the λ_2 values are not even close to 1, which is the sign of incompatible microstructures, in the alloys. Thus, the compatibility between the transforming phases could not be the only reason alone in explaining the initial hysteresis differences in the current alloys. The difference in the dissipation energy at low stress could be attributed to difference in internal twinning characteristics (Fig. 1b, c) and/or formation of partial self accommodated martensite structures.

In the pre-saturation region, the gradual increase in the thermal hysteresis in the NiTiPd–15Hf and NiTiPd–20Hf alloys can be attributed to the increase in the friction between the martensite variants due to increased transformation strain by growing martensite plates. Since the strain was increased, the friction between strain carrying martensite plates also increased resulting in progressively increased hysteresis. On the other hand, the thermal hysteresis of the NiTiPd–10Hf alloy was almost constant in this region in spite of the increasing transformation strain. The difference in the progress of thermal hysteresis in this pre-saturation region could stem from the observed difference in the twinning types of the alloys. The $\langle 011 \rangle_{B19'}$ type II twin was observed in NiTiPd–10Hf, while $(001)_{B19'}$ compound twinning was observed in NiTiPd–15Hf and NiTiPd–20Hf alloys. Compound twins are thinner when they are compared with the type II twins (as shown in Fig. 1), and this may result in more interfaces and increased friction. Furthermore, it is more difficult to de-twin the compound twins which increase the friction during propagation and selection of martensite variants. Previously, the mobility of the (001)-type compound twins in a $Ni_{49.8}Ti_{42.2}Hf_8$ alloys was reported to be less than $\langle 011 \rangle$ type II twins in an equiatomic $Ni_{50}Ti_{50}$ [39]. Thus, the compound twins in NiTiPd–15Hf and NiTiPd–20Hf alloys may cause larger internal friction during the motion of the phase fronts during generation of transformation strain due

to the limited mobility, resulting in progressively increasing dissipation and hysteresis with increasing stress.

In all the alloys, an abrupt increase of the thermal hysteresis in the post-saturation region (>700 MPa) was observed. In this region, the increase in the hysteresis can be mainly attributed to the plastic deformation, which is manifested by the open loops (irrecoverable strain) at the end of the thermal cycles in Fig. 2 and Fig. 3. As the plastic deformation was occurred in the material, the dissipation of energy was increased and so thus the thermal hysteresis.

Isothermal stress–strain behavior

Figure 6 shows the stress–strain responses of the NiTiPd–15Hf alloy at 15 °C. The alloy was in martensite phase (since 15 °C was lower than Mf of 35 °C as shown in Table 1). The specimen was incrementally loaded and unloaded at this temperature up to strain of 8 % and compressive stress of 2100 MPa. The initial linear part of the stress–strain curve shows predominantly elastic deformation of martensite followed by and re-orientation of martensite variants monitored as a plateau-like region. At the end of this region, it could be expected that the material is fully re-oriented. Following the plateau-like region, primarily elastic deformation of martensite is observed. In addition to the elastic deformation, further re-orientation and detwinning of martensite could be expected even though they are less favorable by the applied stress [40], while dislocation slip and deformation twinning of the martensite might also occur [41].

At the last stage, plastic deformation becomes more dominant at the second "yield" point. In this region, dislocation processes and/or deformation twinning are
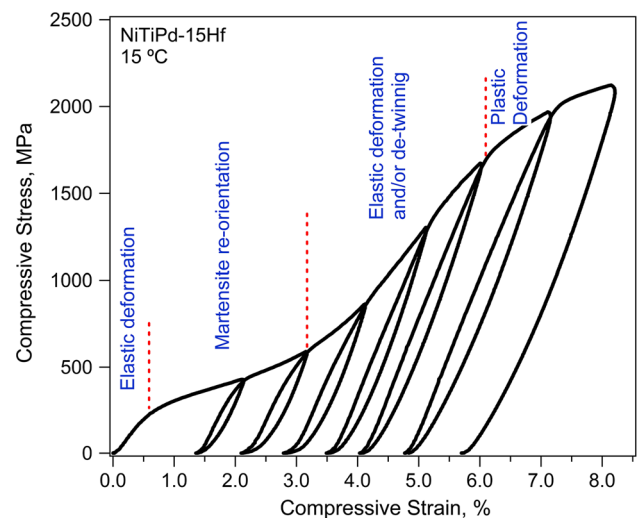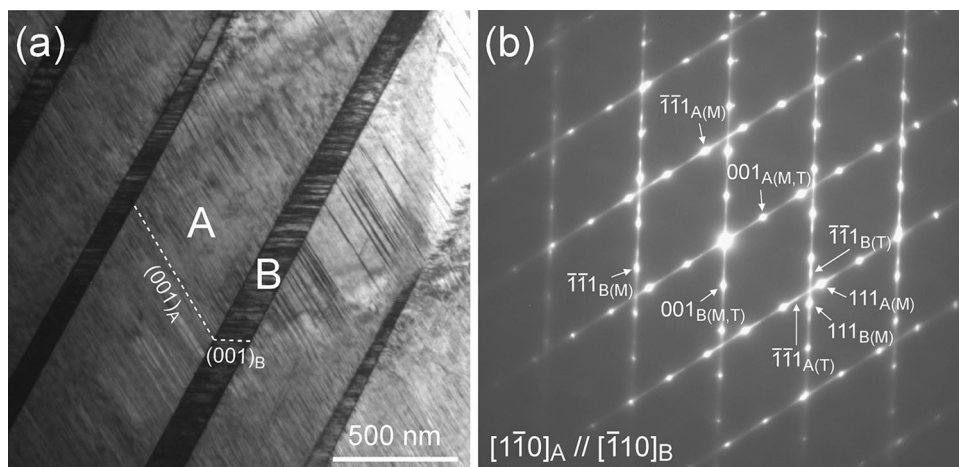

Fig. 6 Stress–strain response of the NiTiPd–15Hf at 15 °C

Fig. 7 **a** Bright-field image obtained at room temperature for the NiTiPd–15Hf alloy deformed at 15 °C and **b** selected area diffraction pattern taken from the interfaces between the martensite plates A and B in (**a**). Subscripts *M* and *T* indicate matrix and $(001)_{B19'}$ compound twin, respectively

expected to dominate the deformation response [40]. Therefore, it is expected that bulk plastic deformation of martensite occurs at relatively high stresses of more than 2 GPa, which is beneficial for biomedical or other industrial applications requiring high strength.

In order to investigate the morphology of re-oriented martensite, TEM observation was conducted at room temperature for NiTiPd–15Hf after the compression tests as shown in Fig. 6. Figure 7a shows a bright-field image of re-oriented martensite variants. Thicker re-oriented martensite plates were frequently observed as compared to the thermally induced martensite (Fig. 1b). The thick martensite variant is considered to be a favorable variant under stress. The selected area diffraction pattern obtained from the interface between the martensite plates A and B in Fig. 7a is shown in Fig. 7b. The twinning in the martensite plates was revealed as $(001)_{B19'}$ compound twin. The boundary between the plates A and B is determined to be $\{111\}_{B19'}$-type boundary [42]. Although the plates A and B are $\{111\}_{B19'}$ type I twin related, the boundary of the plates is not completely parallel to the twinning plane, $\{111\}_{B19'}$, since the plates contain the $(001)_{B19'}$ compound twins that cause crystal rotations in the plates. The boundary slightly rotates from the $(111)_{A(M)}$ plane to the $(\bar{1}\bar{1}1)_{A(T)}$ plane in the plate A and from the $(111)_{B(M)}$ plane to the $(\bar{1}\bar{1}1)_{B(T)}$ plane in the plate B as can be seen in Fig. 7b.

In Fig. 8, compressive stress–strain responses of Ni-TiPd–15Hf are shown at 60 and 90 °C. At 60 °C, full recovery was not observed since the test temperature was below A_f. Upon heating above A_f temperature, the retained strain was completely recovered as shown by the heating (strain-temperature) curve in Fig. 8a.

In Fig. 8b, the sample was incrementally (by 1 %) loaded up to 5 % strain at 90 °C, above A_f. Almost fully reversible

superelastic response was observed even when a stress level of nearly 1400 MPa was applied. When the sample was loaded to 5 % strain and unloaded, irrecoverable strain of 0.3 % was observed. The transformation strain was determined to be 3.1 %. Stress hysteresis, calculated between the loading and unloading curves at 2.5 % (as shown in Fig. 8b), was determined as 635 MPa at 90 °C.

Figure 9 shows the stress–strain behaviors of the Ni-TiPd–20Hf alloy at 200 °C, which are above A_f. As the material was loaded to 2 %, a transformation strain of 0.7 % was obtained at 200 °C. The stress hysteresis calculated at 1 % was 260 MPa at 200 °C. As the compressive strain of 3 % was applied, a full recovery was not realized due to high hardening and plastic deformation.

Two-way shape-memory effect

It is known that TWSME behavior can be observed in SMAs upon generation of anisotropic internal stress by dislocation networks or nucleation sites for martensite by interfaces such as precipitates or retained martensite after certain "training" procedures such as thermal cycling [43, 44], stress cycling [45], or variant re-orientation during isothermal deformation [46, 47].

Figure 10 shows the strain–temperature responses of the NiTiPd–15Hf under 5 MPa after various training conditions. A small stress of 5 MPa was applied to keep the sample in contact with the compression grips during thermal cycling tests. The initial thermal cycling of the material (T-0) did not result in significant strain since the applied stress of 5 MPa was not enough to favor any preferred martensite variants. TWSME after thermal cycling under 700 MPa (T-1) and 1000 MPa (T-2), as shown in Fig. 2, yielded in compressive strain.
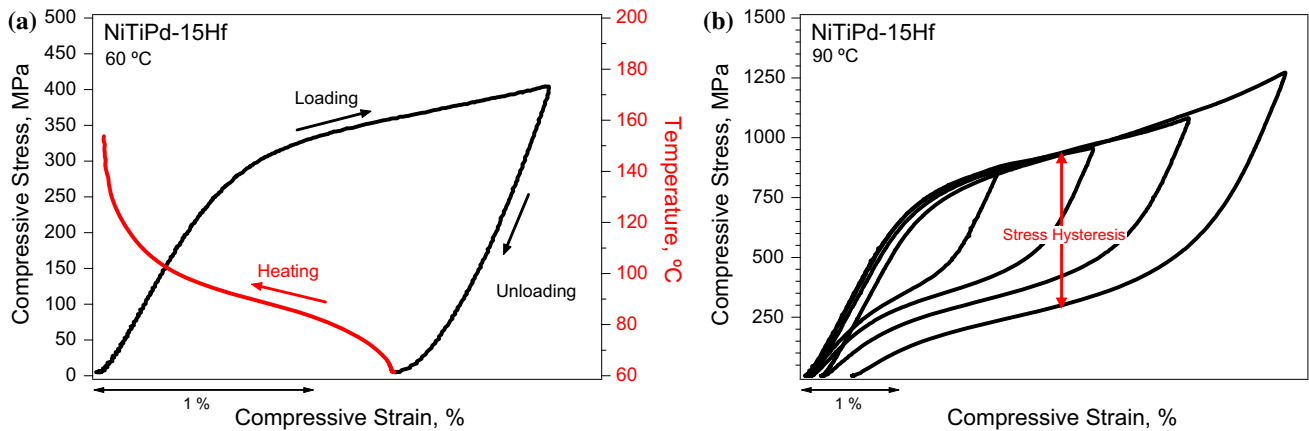
Fig. 8 Stress–strain responses of NiTiPd–15Hf at **a** 60 and **b** 90 °C
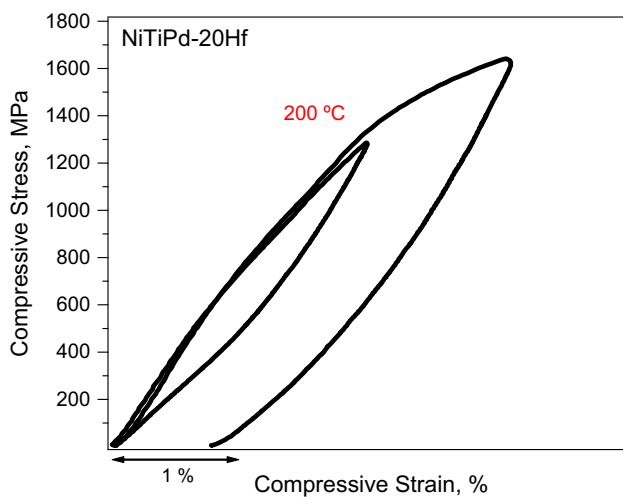

Fig. 9 Stress–strain responses of NiTiPd–20Hf at 200 °C

The TWSME strain in T-1 was 0.6 %, while thermal hysteresis was 45 °C. At T-2, the TWSME strain was 0.5 % and the temperature hysteresis was decreased to 40 °C. It is clear that the TWSME was decreased after the T-2 condition since significant dislocation generation was observed when the bias stress increased from 700 to 1000 MPa as shown in Fig. 2. The decrease in the thermal hysteresis in the T-2 condition can stem from the less volume of transformed material due to increased irrecoverable strain. Moreover, as the material hardens due to plastic deformation, it becomes more difficult to form new defects and dislocations resulting in decreased energy dissipation.

In NiTiPd–20Hf, TWSME strain in T-1 was 0.8 % with a thermal hysteresis of 35 °C. In T-2, TWSME strain was 0.85 % and the temperature hysteresis was decreased to 30 °C, similar to NiTiPd–15Hf alloy. It is clear that there is a huge elastic energy storage (monitored as a larger difference between M_s and M_f in Fig. 10b) during the

transformation in the T-2 case, which could be a result of hard propagation of phase fronts due to generated dislocations after the strain–temperature response at 1000 MPa (Fig. 3b). In comparison, it should be recalled that the NiTiPd–10Hf alloy could develop two-way shape-memory strain of 1.6 % without an intense training process [25], owing to larger internal stress and/or larger volume of favored martensite plates resulting in higher TWSME strain compared to the other alloys.

Work output

In Fig. 11, work output levels for the NiTiPd–10Hf, Ni-TiPd–15Hf, and NiTiPd–20Hf alloys are shown as a function of applied stress. The work output can be expressed as the mathematical product of the reversible strain and applied stress obtained from the strain–temperature responses. As the applied stress increased, the work output also increased due to an increment in reversible strain and stress.

In the NiTiPd–10Hf alloy, work output was 0.2 J cm^{-3} under 25 MPa and reached a maximum value of 29 J cm^{-3} under 700 MPa [25]. As for the current alloys, the work output was 0.075 J cm^{-3} under 25 MPa and reached a maximum value of 30 J cm^{-3} under 1000 MPa in the Ni-TiPd–15Hf alloy. The work output values were 5 and 20 J cm^{-3} at the compressive stress levels of 100 and 1000 MPa, respectively, in NiTiPd–20Hf. As the applied stress increased further to 1000 MPa, the work output decreased to 25 J cm^{-3} due to a lower reversible strain of only 2.5 % [25].

In comparison, the NiTiPd–10Hf alloy has nearly comparable work output to a previously studied extruded $Ni_{45.3}Ti_{29.7}Hf_{20}Pd_5$ alloy, which is capable of 32–35 J cm^{-3} [21]. Binary NiTi alloys can generally provide work outputs of 10–20 J cm^{-3} [48], while Ni-rich NiTiHf alloys can produce around 18–20 J cm^{-3} [19, 20].

Fig. 10 The constant stress–strain–temperature responses of the as-homogenized and trained $Ni_{45.3}Ti_{39.7}Hf_{15}Pd_5$ and NiTiPd–20Hf alloys at 5 MPa
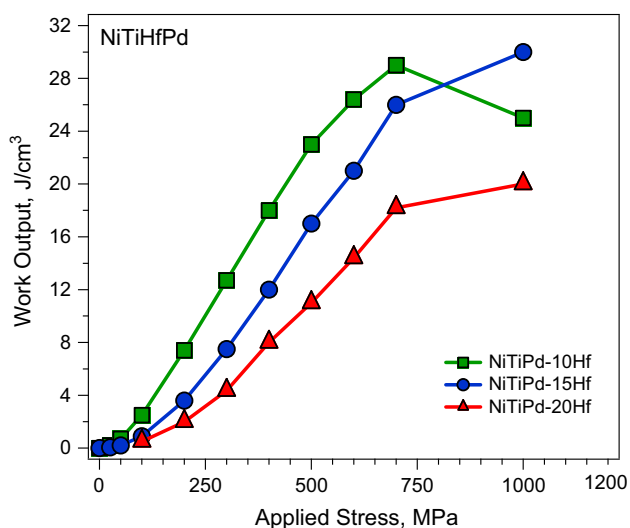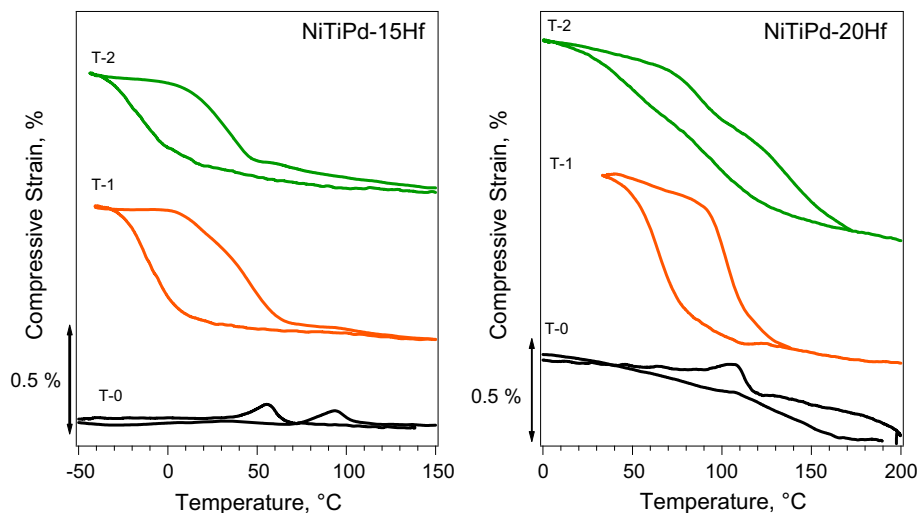

Fig. 11 Work output and transformation strain values as a function of applied compressive stress for the NiTiPd-20Hf, NiTiPd–15Hf and NiTiPd–10Hf alloys

Finally, NiTiPd and NiTiPt alloys can yield work outputs of 9–15 J cm^{-3} at temperatures above 150 °C [49, 50]. However, it should be noted that the upper temperature capability is limited in NiTiHfPd alloys compared to more conventional ternary NiTi–X (X = Hf, Pd, Pt) high-temperature SMAs. High work output levels were realized in the NiTiHfPd alloys owing to high stress capability and good transformation strain.

Conclusions

The shape-memory properties of $Ni_{45.3}Ti_{34.7}Hf_{15}Pd_5$ and $Ni_{45.3}Ti_{29.7}Hf_{20}Pd_5$ polycrystalline SMAs were investigated through evaluation of the strain–temperature response (shape-memory behavior) and isothermal stress–strain responses

(superelastic behavior). The $Ni_{45.3}Ti_{34.7}Hf_{15}Pd_5$ alloy exhibited shape-memory response with 3.8 % maximum transformation strain at 700 MPa, while 2.6 % maximum strain was possible in the $Ni_{45.3}Ti_{29.7}Hf_{20}Pd_5$ at the same stress level. The $Ni_{45.3}Ti_{34.7}Hf_{15}Pd_5$ and $Ni_{45.3}Ti_{29.7}Hf_{20}Pd_5$ alloys exhibited two-way shape-memory strains of 0.6 and 0.8 %, respectively, after thermal cycling experiments under 700 MPa. In $Ni_{45.3}Ti_{34.7}Hf_{15}Pd_5$, superelastic response with transformation strain of 3.1 % was observed at 90 °C with nearly complete recovery of applied strain of 5 % at a stress level of 1400 MPa. In $Ni_{45.3}Ti_{29.7}Hf_{20}Pd_5$, high hardening was observed in the stress–strain behavior at a high temperature of 200 °C, resulting in a limited superelasticity. The maximum work outputs of $Ni_{45.3}Ti_{34.7}Hf_{15}Pd_5$ and $Ni_{45.3}Ti_{29.7}Hf_{20}Pd_5$ were of 30 and 20 J cm^{-3}, respectively, achieved at a stress level of 1000 MPa. As the Hf content was increased, the transformation strain was decreased and the volume of crystal structures was expanded. The differences between the evolutions of the thermal hysteresis with the applied stress were linked to the difference in twinning types. A progressively increasing hysteresis with the applied stress in the strain–temperature response was observed in the compound twinned $Ni_{45.3}Ti_{34.7}Hf_{15}Pd_5$ and $Ni_{45.3}Ti_{29.7}Hf_{20}Pd_5$ alloys in contrast to type II twinned $Ni_{45.3}Ti_{39.7}Hf_{10}Pd_5$ alloy.

References

1. Funakubo H (1987) Shape Memory Alloys, Volume 1 of Precision machinery and robotics, Taylor and Francis
2. Leo DJ (2007) Engineering analysis of smart material systems. Wiley, New Jersey

3. Chung DDL (2001) Review: materials for vibration damping. J Mater Sci 36:5733–5737. doi:10.1023/A:1012999616049

4. Karaca HE, Saghaian SM, Tobe H, Acar E, Basaran B, Nagasako M et al (2014) Diffusionless phase transformation characteristics of $Mn_{75.7}Pt_{24.3}$. J Alloy Compd 589:412–415

5. Noebe RBT, Padula SA, Srivatsan TS (2007) NiTi-based high-temperature shape-memory alloys: properties, prospects, and potential applications. In: Soboyejo WO (ed) Advanced structural materials: properties, design optimization, and applications. Taylor & Francis Group, Boca Raton, pp 145–186

6. LeBlanc L (2001) Part I - 'Smart metals' providing actuation, sealing, and completion functions downhole. Offshore 61:58–59

7. LeBlanc L (2002) Part II - 'Smart metals' providing actuation, sealing, and completion functions downhole. Offshore 62:54–56

8. Otsuka K, Wayman CM (1998) Shape memory materials. Cambridge University Press, Cambridge

9. Valiev RZ, Gunderov DV, Lukyanov AV, Pushin VG (2012) Mechanical behavior of nanocrystalline TiNi alloy produced by severe plastic deformation. J Mater Sci 47:7848–7853. doi:10.1007/s10853-012-6579-8

10. Hartl DJ, Lagoudas DC (2007) Aerospace applications of shape memory alloys. Proc Inst Mech Eng [G] 221:535–552

11. Otsuka K, Ren XB (1999) Recent developments in the research of shape memory alloys. Intermetallics 7:511–528

12. Machado LG, Savi MA (2003) Medical applications of shape memory alloys. Braz J Med Biol Res 36:683–691

13. Zhao T, Yang R, Zhong C, Li Y, Xiang Y (2011) Effective inhibition of nickel release by tantalum-implanted TiNi alloy and its cyto-compatibility evaluation in vitro. J Mater Sci 46:2529–2535. doi:10.1007/s10853-010-5104-1

14. Jan VH (1999) Non-medical applications of shape memory alloys. Mater Sci Eng A 273–275:134–148

15. Otsuka K, Ren X (2005) Physical metallurgy of Ti–Ni-based shape memory alloys. Prog Mater Sci 50:511–678

16. Ma J, Karaman I, Noebe RD (2010) High temperature shape memory alloys. Int Mater Rev 55:257–315

17. Karaca HE, Acar E, Tobe H, Saghaian SM (2014) NiTiHf-based shape memory alloys. Mater Sci Technol 30:1530–1544

18. Meng XL, Cai W, Zheng YF, Tong YX, Zhao LC, Zhou LM (2002) Stress-induced martensitic transformation behavior of a Ti–Ni–Hf high temperature shape memory alloy. Mater Lett 55:111–115

19. Bigelow GS, Garg A, Padula SA II, Gaydosh DJ, Noebe RD (2011) Load-biased shape-memory and superelastic properties of a precipitation strengthened high-temperature $Ni_{50.3}Ti_{29.7}Hf_{20}$ alloy. Scripta Mater 64:725–728

20. Karaca HE, Saghaian SM, Basaran B, Bigelow GS, Noebe RD, Chumlyakov YI (2011) Compressive response of nickel-rich NiTiHf high-temperature shape memory single crystals along the [111] orientation. Scripta Mater 65:577–580

21. Karaca HE, Acar E, Ded GS, Basaran B, Tobe H, Noebe RD et al (2013) Shape memory behavior of high strength NiTiHfPd polycrystalline alloys. Acta Mater 61:5036–5049

22. Karaca HE, Acar E, Basaran B, Noebe RD, Chumlyakov YI (2012) Superelastic response and damping capacity of ultrahigh-strength [111]-oriented NiTiHfPd single crystals. Scripta Mater 67:447–450

23. Acar E, Karaca HE, Basaran B, Yang F, Mills MJ, Noebe RD et al (2013) Role of aging time on the microstructure and shape memory properties of NiTiHfPd single crystals. Mater Sci Eng A 573:161–165

24. Karaca HE, Acar E, Basaran B, Noebe RD, Bigelow G, Garg A et al (2012) Effects of aging on [111] oriented NiTiHfPd single crystals under compression. Scripta Mater 67:728–731

25. Acar E, Karaca HE, Tobe H, Noebe RD, Chumlyakov YI (2013) Characterization of the shape memory properties of a $Ni_{45.3}Ti_{39.7}Hf_{10}Pd_5$ alloy. J Alloy Compd 578:297–302

26. Pu ZJ, Tseng H-K, Wu K-H (1994) An innovative system of high temperature shape memory alloys. SPIE, Orlando, p 2189

27. Kumar PK, Lagoudas DC (2008) Introduction to shape memory alloys. In: Lagoudas DC (ed) Shape memory alloys. Springer, New York, pp 1–51

28. Sehitoglu H, Hamilton R, Maier HJ, Chumlyakov Y (2004) Hysteresis in NiTi alloys. J Phys IV Fr 115:3–10

29. Hamilton RF, Sehitoglu H, Chumlyakov Y, Maier HJ (2004) Stress dependence of the hysteresis in single crystal NiTi alloys. Acta Mater 52:3383–3402

30. Cui J, Chu YS, Famodu OO, Furuya Y, Hattrick-Simpers J, James RD et al (2006) Combinatorial search of thermoelastic shape-memory alloys with extremely small hysteresis width. Nat Mater 5:286–290

31. Delville R, Kasinathan S, Zhang ZY, Van Humbeeck J, James RD, Schryvers D (2010) Transmission electron microscopy study of phase compatibility in low hysteresis shape memory alloys. Philos Mag 90:177–195

32. James RD, Hane KF (2000) Martensitic transformations and shape-memory materials. Acta Mater 48:197–222

33. Zarnetta R, Takahashi R, Young ML, Savan A, Furuya Y, Thienhaus S et al (2010) Identification of quaternary shape memory alloys with near-zero thermal hysteresis and unprecedented functional stability. Adv Funct Mater 20:1917–1923

34. Zhang ZY, James RD, Muller S (2009) Energy barriers and hysteresis in martensitic phase transformations. Acta Mater 57:4332–4352

35. Bhattacharya K, Conti S, Zanzotto G, Zimmer J (2004) Crystal symmetry and the reversibility of martensitic transformations. Nature 428:55–59

36. Lexcellent C, Blanc P, Creton N (2008) Two ways for predicting the hysteresis minimisation for shape memory alloys. Mater Sci Eng A 481–482:334–338

37. Bhattacharya K (1993) Comparison of the geometrically non-linear and linear theories of martensitic transformation. Contin Mech Thermodyn 5:205–242

38. Hane KF, Shield TW (1999) Microstructure in the cubic to monoclinic transition in titanium-nickel shape memory alloys. Acta Mater 47:2603–2617

39. Dalle F, Perrin E, Vermaut P, Masse M, Portier R (2002) Interface mobility in $Ni_{49.8}Ti_{42.2}Hf_8$ shape memory alloy. Acta Mater 50:3557–3565

40. Liu Y, Xie Z, Van Humbeeck J, Delaey L (1999) Deformation of shape memory alloys associated with twinned domain re-configurations. Mater Sci Eng A 273–275:679–684

41. Stebner AP, Vogel SC, Noebe RD, Sisneros TA, Clausen B, Brown DW et al (2013) Micromechanical quantification of elastic, twinning, and slip strain partitioning exhibited by polycrystalline, monoclinic nickel–titanium during large uniaxial deformations measured via in situ neutron diffraction. J Mech Phys Solids 61:2302–2330

42. Meng XL, Cai W, Fu YD, Zhang JX, Zhao LC (2010) Martensite structure in Ti–Ni–Hf–Cu quaternary alloy ribbons containing (Ti, Hf)2Ni precipitates. Acta Mater 58:3751–3763

43. Contardo L, Guénin G (1990) Training and two way memory effect in Cu–Zn–Al alloy. Acta Metall Mater 38:1267–1272

44. Liu Y, McCormick PG (1990) Factors influencing the development of two-way shape memory in NiTi. Acta Metall Mater 38:1321–1326

45. Nagasawa A, Enami K, Ishino Y, Abe Y, Nenno S (1974) Reversible shape memory effect. Scr Metall 8:1055–1060

46. Perkins J, Sponholz R (1984) Stress-Induced Martensitic Transformation Cycling and Two-Way Shape Memory Training in Cu-Zn-Al Alloys. Metallurgical and Materials Transactions A 15:313–321

47. Benafan O, Padula SA II, Noebe RD, Sisneros TA, Vaidyanathan R (2012) Role of B19′ martensite deformation in stabilizing two-way shape memory behavior in NiTi. J Appl Phys 112:093510

48. Grummon D (2003) Thin-film shape-memory materials for high-temperature applications. JOM 55:24–32

49. Noebe R, Gaydosh D, II SP, Garg A, Biles T, Nathal M. (2005) Properties and potential of two (Ni, Pt)Ti alloys for use as high-temperature actuator materials. SPIE Conf Proc 5761:364–375

50. Bigelow G, Padula S, Garg A, Gaydosh D, Noebe R (2010) Characterization of ternary NiTiPd High-temperature shape-memory alloys under load-biased thermal cycling. Metall Mater Trans A 41:3065–3079